CW-pumped polarization-maintaining Brillouin fiber ring laser: I. Self-structuration of Brillouin solitons

Jean Botineau, Gérard Cheval, Carlos Montes

HAL Id: hal-00460390
https://hal.science/hal-00460390

Submitted on 28 Feb 2010

CW-pumped polarization-maintaining
Brillouin fiber ring laser:
I. Self-structuration of Brillouin solitons.

Jean Botineau, Gérard Cheval, and Carlos Montes[*]

Centre National de la Recherche Scientifique

Laboratoire de Physique de la Matière Condensée

Université de Nice - Sophia Antipolis, Parc Valrose,

F-06108 Nice Cedex 2, France

Abstract

Stimulated Brillouin scattering (SBS) of a cw-pump in a low optical fiber ring cavity generates for a given gain G - below a critical feedback R_{crit} - a backward soliton Stokes pulse at the roundtrip repetition rate, through resonant three-wave interaction between the optical pump wave and backward Stokes wave, and a high frequency (GHz) axial acoustic wave. In Part I, we perform a systematic experimental and numerical exploration of the whole soliton localisation domain for a large set of (G, R) parameters, in a polarization-maintaining Brillouin fiber ring laser in the best conditions of stability and coherence, and we confirm the excellent quantitative agreement of the coherent three-wave model and the experiments.

1. Introduction

The three-wave coherent model we have introduced several years ago for the description of stimulated Brillouin scattering (SBS) in single-mode optical fiber resonators [1], derived from the model developed for fluids [2] [3], has been the tool for finding Brillouin soliton self-structuration [4] - [6], and has been now largely adopted by the scientific community [7], because it gives simple explanations of features such that the finite Brillouin gain bandwidth [8], generation of Stokes pulses called *dissipative Brillouin solitons* [4] in the fiber ring cavity, the bifurcation between the stationary *Brillouin mirror* and the pulsed dynamics in the cw-pumped fiber cavity leading to stable soliton pulses [5], and quantitative agreement with the experiments in the whole self-pulsing domain [6], which are elsewhere impossible to describe through the older incoherent model of intensity equations [9]. The two governing ideas of this coherent model are that (1.) the Brillouin interaction operates through amplitude but also *phase relations* between optical and acoustic components, and (2.) a crucial role is assigned to *material memory - i.e.* the finite acoustic damping time - through dispersion - *i.e.* in the present case the counter-propagative behavior of Brillouin scattering and the quasi motionless nature (compared to light) of the acoustic waves.

In this paper, our purpose is to extensively demonstrate the excellent quantitative agreement of this coherent model with the experiments performed in a polarization-maintaining Brillouin fiber ring laser in good conditions of stability and coherence. Polarization dynamics in a Brillouin fiber ring laser may lead to unstable behaviors, as has been shown for a short-length cavity [10]. We perform a systematic experimental and numerical exploration of the whole soliton localisation domain, in a single-transverse mode cw-pumped optical fiber ring cavity, for a large set of pump power levels and cavity Q-factors. In each case studied here, we show the adequation between simulation and experimental results and we therefore confirm the pertinence of the three-wave coherent model for SBS.

Stimulated Brillouin backscattering of a coherent cw-pump in single-transverse mode optical fiber cavities generates backward-propagating Stokes pulses through three-wave resonant interaction with the electrostrictively excited longitudinal GHz hypersound waves induced in the fiber core. These *dissipative solitons* self-structurate in a fiber ring cavity below a critical feedback R_{crit} [5] [6] when the length L of the cavity is large enough to admit a large number of longitudinal cavity modes N beneath the Brillouin gain curve $[L \gg (n\Delta\nu_B/c)^{-1}]$. For a given gain $G = g_B I_p L$, where g_B is the Brillouin gain coefficient and I_p the cw-pump intensity, one obtains three stable asymptotic regimes depending on the feedback R:

(i) *pulsed Brillouin soliton regime*, for $R_{thres} < R < R_{pul}$;

(ii) *oscillatory regime*, for $R_{pul} < R < R_{crit}$; and

(iii) *stationary Brillouin mirror regime*, for $R > R_{crit}$.

The Hopf bifurcation of the Brillouin cw-regime to the pulse-regime [5] has been associated to a kind of modulation instability [11].

We have experimentally and numerically determined the whole soliton localisation domain as function of I_p and R for different pump wavelengths λ_p, from visible to infrared, and different cavity lengths L in non polarization-maintaining fiber-ring cavities [6].

For the experiment described in this paper, we have built a Brillouin single-mode fiber and single-directional ring cavity by using single-mode fiber components only and a polarization-maintaining fiber, leading thus to more stability than in previous experiments. We have performed a systematic exploration of the experimental features for a large set of (G, R) parameters. In order to enhance the Brillouin scattering coherent features - which are increasing with the acoustic damping length - we have chosen to work in the infrared range, at $\lambda_p = 1.319$ μm, which is associated with a *low* acoustic frequency (equal to the Stokes spectral shift) of 13 GHz, with the homogeneous broadening width $\Delta\nu_B = 23$ MHz, *i.e.* a *long* damping time of 14 ns. After a description of the experimental set-up, the results are presented. Then, after a brief recalling of our theoretical model, we show that the experiments accurately agree with the numerical results.

2. Experimental set-up

The experiment (figure 1) is built around a $L = 253$ m single-mode and polarization preserving fiber (14) of attenuation $\alpha = 1$ dB/km (Fibercore Ltd). A far field analysis at the wavelength $\lambda_p = 1.319$ μm led to the mode radius $r = 2.8$ μm, and measurements in stationary conditions yield the Brillouin gain coefficient $g_B = 1.65 \times 10^{-11}$ m/W. This value is significantly lower than the vitreous silica coefficient, which we explain by the fiber core germanium doping, making impossible phase matching between optical and acoustic wavevectors throughout the fiber transverse section.

The Brillouin laser cavity is a one-directional ring occupied in its major part by the fiber, prolongated on each side by some meters of fiber supporting the two polarization controllers (13) and (17) and the fiber coupler (10), which turns aside 10% of pump and Stokes signals for measurement (11 and 12). Coupling with the main fiber is achieved through the microhandlers (15) and (16), the last one allowing the adjustement of the cavity recoupling coefficient without changing the coupled pump power value.

The cw pump signal comes from the source (1): a diode pumped YAG:Nd^{+++} laser delivering 340 mW at the wavelength $\lambda_p = 1.319$ μm and cooled by conduction, which ensures a very good stability ($\simeq 10$ kHz). At the laser output, the Faraday isolator (2) prevents any perturbative backscattering, and the half-wave plate (3) determines the polarization orientation. The pump wave is then coupled through the long distance working length lens (4) (anti-reflection coated at 1.3 μm) in the fiber (5) with an efficiency of roughly 70%. The microhandler (6) allows to adjust the pump power value in the input fiber (7).

The pump signal is coupled into the ring cavity by the first input of the 3-port circulator (8), and then sent to the up-stream fiber (9) through the port 2. The coupler (10) takes 10% of this signal for measurement in (11) by a power-meter, whereas the main part is coupled through the microhandler (15) in the main fiber (14) with its optical po-

larization orientated along one of the neutral axis. After the fiber (14), the pump signal is stopped at the port 3 of the circulator, preventing thus any perturbation of the input pump signal.

Above a pump power threshold, stimulated Brillouin scattering gives rise in the fiber to a backscattered Stokes wave coming back to the coupler (10) [which turns aside 10% of the Stokes signal for measurement in (12)] and to the port 2 of the circulator (8). The Stokes signal is then coupled at the other end of the fiber through the port 3 of the circulator and the microhandler (16). The adjustment of the Stokes optical polarization along the same neutral axis as the pump is achieved by the polarization controller (17), and the recoupling value of the ring cavity by adjusting the microhandler (16).

The fiber (14) is the only component manufacturingly designed for linear polarization-maintaining. As the Brillouin gain is depending on the polarization, the purposes of controllers (13) and (17) are to ensure the proper polarization for the pump and Stokes components. The optical circulator (8) is not sensitive to the polarization, and we have checked that, in the air-conditioned environment of the laboratory, polarization configuration was maintained as long as the different fiber pieces were not touched. Set-up adjustment is carried out by the following procedure:

(i.) At first, with the ring open, the half-wave plate (3) and the polarization controller (13) are adjusted such that the pump polarization will be linear in (15).

(ii.) Afterwards the fiber (14) neutral axis are orientated to get a linear and stable polarization in (16), which ensures the pump wave polarization to be orientated along one of the neutral axis of the fiber (with an extinction rate of $\simeq 1\%$).

(iii.) The ring is then closed by obtaining in (12) the backward signal, which is maximized by adjusting the polarization controller (17): the Stokes wave is now linearly polarized in the fiber (14) along the same neutral axis as the pump.

Additional measurements yielded an energetic transmission coefficient between the circulator ports 2 and 3 of 0.46, including the welding points, and the transmission in (15) is optimized with the addition of an index liquid at 0.72.

The Stokes signal measurement is performed in (12) by a GaInAs photodetector with a bandwidth of either 250 or 500 MHz, depending on the measurement conditions. In the case of a stationary signal, a mechanical chopper is interposed between the fiber and the detector; in these stationary conditions the Stokes detection is calibrated with a power-meter in order to determine the absolute value of the optical scattered power.

3. Experimental results

With such a long fiber, the ring free spectral range is roughly 800 kHz, to be compared to the Brillouin gain bandwidth, larger than 23 MHz: this Brillouin laser may therefore involve a large number of longitudinal modes. Following the diagram 3 of Ref.[6], the generic features of such a ring are summarized on figure 2, with along the horizontal scale the gain parameter $G = g_B I_0 L$ (where g_B is the fiber Brillouin gain coefficient, I_0 the pump intensity at the entrance (15) of the fiber and L its effective length) and along the vertical scale the ring energetic Stokes recoupling coefficient R (in logarithmic scale). Under the straight line determined by $R = \mathrm{e}^{-G}$, Stokes losses exceed the gain, and the pump propagates along the fiber in the linear regime. For the highest values of R and G, the Brillouin laser works in a stationary regime, *i.e.* on a single longitudinal mode. Between these two domains, other longitudinal modes are involved and phase-locked: the Stokes wave is then structured in pulses of roughly 100 ns width. Note that by going from the cw-regime to the pulse-regime, it is the adjacent mode which is at first destabilized for $G < 7$, but the following second longitudinal mode beyond this limit (which corresponds to the two close bifurcation limits drawn on figure 2).

Note that this diagram corresponds to a fiber without Stokes attenuation and for ring recoupling losses localised in one point only. In the actual experiment, fiber attenuation is 1dB/km, and recoupling losses are distributed between the circulator (8), some welding points, the fiber coupler (10) and the microhandlers (15) and (16). We may however consider this diagram to be representative, taking as recoupling coefficient the effective

value $R = R_{eff}$ given by the experimental Brillouin nonlinear threshold.

We have experimentally explored 6 zones (the tinted areas on figure 2), each of them corresponding to a particular adjustment of the microhandler (16), the feedback values being given in Table I.

Table I. Feedback parameters for the six explored zones

Series	1	2	3	4	5	6
R_{eff}	1.50×10^{-1}	5.93×10^{-2}	2.25×10^{-2}	8.23×10^{-3}	1.94×10^{-3}	2.62×10^{-4}
$\rho = \sqrt{R_{eff}}$	3.87×10^{-1}	2.43×10^{-1}	1.50×10^{-1}	9.07×10^{-2}	4.41×10^{-2}	1.62×10^{-2}

The experimental pulses, characterized by a width between 70 and 250 ns, exhibit a shape roughly no dependent on experimental conditions (figure 3). They are always presenting a slight dissymmetry, with a rear front longer than the leading one. In every case, their area (and then the pulse energy) may be determined by:

$$\text{Area} \simeq 1.17 \times \text{peak value} \times \text{FWHM width}$$

These pulses, so-called *Brillouin quasi-solitons*, or *Brillouin dissipative solitons* [4], result from the competition between nonlinear interaction and acoustic damping. Reasoning here only with the Brillouin gain in a two-wave intensity problem would yield to an endless compression with time, in contradiction with experiment. It can be understood only by involving both Stokes and anti-Stokes Brillouin processes, combined with the finite acoustic damping in a three-wave interaction [5].

When the pump power is decreasing from the cw-zone towards the Brillouin threshold, a Stokes generic behavior is observed which is qualitatively no dependent on the recoupling factor R_{eff}. At the bifurcation point appears a periodic modulation of the Stokes signal, either at a frequency equal to the cavity free spectral range for the large values of R_{eff}, or at twice this frequency when R_{eff} is lower (figure 4) in agreement with the stability analysis [6]. When the pump power is still decreasing, these oscillating regimes

7

are replaced by a pulsed regime with a frequency close to the ring FSR. Figure 5 shows in particular how these pulses are built from the second mode destabilization.

When the pump power is still decreasing, there is a fast strengthening of the Stokes pulses, which becomes much narrower. Note that this zone is extremely unstable, with large fluctuations of both amplitude and width of the pulses, maintaining only the energy per pulse. Figure 6 illustrates this scenario.

Lastly, when the pump power decreases again from this value towards the nonlinear threshold, there is a large zone much more stable, with a progressive pulse weakening and broadening (figure 7). Note that the close threshold vicinity is again characterized by strong experimental instabilities.

In order to get a quantitative view of these results, we present on the same graphs the results relative to each value of R_{eff} (referenced by circled numbers). In each case, experimental data have been fitted by the 4th-order polynomial which minimizes the mean square root. Figure 8 shows thus the Stokes peak power *vs.* pump power (fig.8 left) and *vs.* pulse energy (fig.8 right).

Note in particular that the left part of these curves follow the same linear function *vs.* pump power or energy per pulse for the different values of R_{eff}, and that the strongest pulses are obtained for the weakest values of R_{eff} (taking into account that curves (4) to (6) do not reach the bifurcation).

Figure 9 shows now the Stokes energy per pulse *vs.* pump power. Starting from the nonlinear threshold, it follows a linear evolution no dependent on R_{eff}, the lowest values of which lead to the most energetic pulses.

4. Theoretical simulation of the Brillouin interaction

In such a single transversal mode set-up, stimulated Brillouin scattering is accurately described by the coupled 1-D system [1] [6]:

$$\left(\partial_t + \frac{c}{n}\partial_z + \gamma_e\right)A_p = -K_B A_S A_a + iK_K\left(|A_p|^2 + 2|A_S|^2\right)A_p$$
$$\left(\partial_t - \frac{c}{n}\partial_z + \gamma_e\right)A_S = K_B A_p A_a^* + iK_K\left(2|A_p|^2 + |A_S|^2\right)A_S \tag{1}$$
$$\left(\partial_t + \gamma_a\right)A_a = K_B A_p A_S^*$$

with the boundary conditions

$$A_p(0,t) = A_{cw} \quad ; \qquad A_s(0,t) = \sqrt{R}A_s(L,t), \tag{2}$$

where the pump and Stokes waves propagating along the z-axis fiber are associated to the electric field amplitudes $A_p(z,t)F(x,y)$ and $A_S(z,t)F(x,y)$, the transverse function $F(x,y)$ being the fiber modal profile. The Brillouin coupling constant is then :

$$K_B = \sqrt{\frac{g_B \gamma_a \int\int F^4 dxdy}{4\mu_0 \int\int F^2 dxdy}} \tag{3}$$

where $g_B = 1.65 \times 10^{-11}$ m/W is the fiber Brillouin gain constant, $\gamma_a \simeq 7.2 \times 10^7 \text{s}^{-1}$ the acoustic damping constant at 13 GHz, and γ_e the optical damping constant of the fiber corresponding to an attenuation of 1 dB/km ($\gamma_e = 2.4 \times 10^4$ s^{-1}). The *electrostrictive field* $A_a(t,z)$ is proportional to the acoustic amplitude and is also depending on the fiber modal profile. Each of the two optical equations is elsewhere involving an optical Kerr term which acts here as a small perturbation, the coupling constant of which being given by:

$$K_K = \frac{\pi n_2 c}{n\lambda}\frac{\int\int F^4 dxdy}{\int\int F^2 dxdy} \tag{4}$$

where $n_2 = 1.2 \times 10^{-22}$m^{2}V^{-2} is the silica self-focusing coefficient and $\lambda = 1.319$ μm the optical wavelength.

5. Comparison between experimental and numerical results

In order to show the excellent agreement between the experimental results and the results obtained by numerical simulation of Eqs.(1), we perform a parallel systematic numerical study for the same six feedback series. Moreover, the numerical study is not limited by pump power for small feedback values and we can explore the whole bifurcation domain between pulsing and stationarity for all the above six feedback values. In order to achieve comparison between the experimental and the numerical results in the most general frame, the former experimental results will be now presented with some modifications. Figure 10(left) shows thus the peak Stokes field at the fiber input [point (15) of the experimental set-up] normalized by the pump field in the same point *vs.* pump power in this point. Taking into account that there is no enough available power to reach the bifurcation for the curves (4) to (6); these curves appear very similar and may be deduced one from another by affinity. Figure 10(right) shows the same normalized Stokes field *vs.* pulse energy normalized by the pump power in the same point (15) of the set-up; these last curves appear to be roughly no dependent on R_{eff}. The corresponding numerical results are plotted in figure 11 in normalized units: Stokes peak amplitude at $z = 0$ *vs.* pump power (left) and *vs.* mean Stokes reflectivity $\langle |A_S(0,t)|^2 \rangle / |A_p(0)|^2$ (right). Now, the absence of constraint for the pump power allow us to explore the whole curves (1) to (6).

In the same way, figure 12 shows the normalized Stokes pulse energy in (15) *vs.* pump power in this point; the pulse energy appears here to grow faster for the higher values of R_{eff}. The corresponding numerical curves are plotted in figure 13.

In order to quantitatively appreciate the optical energy localisation associated to the Stokes pulses, figure 14 groups the whole experimental results obtained in the pulsed range [(1) to (6) series] and in the stationary (or cw) range [(1) to (3) series] *vs.* pump power in the point (15) of the experimental set-up. Each R_{eff} value is associated to two curves: the top curve corresponds to the Stokes amplitude square value averaged on a roundtrip

time, which is therefore proportional to the averaged power in this point; in accordance with §**4**. notations, it is designated by $\langle|A_S|^2\rangle$. The bottom curve gives the variation of the square of the averaged Stokes amplitude $\langle|A_S|\rangle^2$ in (15), which is a measurement of the pulse confinement; in stationary conditions, we have obviously $\langle|A_S|^2\rangle = \langle|A_S|\rangle^2$, but in the best pulsed regime, roughly:

$$\frac{\langle|A_S|\rangle^2}{\langle|A_S|^2\rangle} \simeq \frac{\text{roundtrip time}}{\text{pulse width}} \simeq 10$$

Figure 14 shows in particular [case (1) to (3)] that there is no experimental appreciable rupture of the scattered power at the bifurcation point between the stationary and the pulsed regimes.

The corresponding numerical results are plotted in figure 15. Now, the whole localisation domain can be explored by the numerical model from threshold to the stationary state for the six feedback values [(1) to (6)]. Table II. shows the numerical values for case (4) $[R = 0.00823; \rho = \sqrt{R} = 0.0907]$, and the quantitative point of the bifurcation between pulsed and stationary regimes. We shall see for this case, in Part II. paper, that even in the *stationary regime* for $G = 14$ we may obtain a train of stable compressed pulses when the cw-pumped Brillouin cavity is stimulated by an intracavity phase modulator at particular frequencies.

11

Table II. Pulse Characteristics (numerical) for the Nd:YAG cw-Pumped Brillouin Fiber Ring Laser for $R = 8.23 \times \times 10^{-3}$; $\rho = \sqrt{R} = 0.0907$

G	P(mW)	$|A_S|_{pulse}$	$|A_S|^2_{pulse}$	$\delta_t|A_S|/t_r$	$\delta_t|A_S|^2/t_r$	Δ_t/t_r	$\langle|A_S|^2\rangle$	$\langle|A_S|\rangle^2$
5.00	28.465	2×10^{-9}	4×10^{-18}	1.000000	1.000000	1.000000	0.000003	0.000002
5.50	31.312	0.535328	0.286576	0.326050	0.293701	1.021119	0.113163	0.079737
6.00	34.158	1.111239	1.234852	0.209961	0.185425	1.018102	0.210640	0.089200
6.50	37.005	1.523133	2.319934	0.163696	0.143433	1.015802	0.291748	0.093916
7.00	39.852	1.856271	3.445742	0.137329	0.119751	1.013850	0.360081	0.097387
7.50	42.698	2.132531	4.547688	0.121216	0.106079	1.012010	0.418389	0.100774
8.00	45.545	2.358795	5.563913	0.110840	0.097168	1.010114	0.468676	0.104727
8.50	48.391	2.535981	6.431199	0.104736	0.091187	1.008103	0.512431	0.109822
9.00	51.238	2.660495	7.078233	0.102295	0.087402	1.005834	0.550679	0.116683
9.50	54.084	2.723289	7.416307	0.102905	0.088867	1.003149	0.584730	0.126785
10.00	56.931	2.705722	7.321050	0.108887	0.092896	0.999695	0.614376	0.142662
10.50	59.778	2.561017	6.558808	0.125244	0.106934	0.994454	0.640855	0.173756
11.00	62.624	2.050680	4.205288	0.182129	0.156738	0.982330	0.660066	0.280149
11.50	65.471	0.893942	0.799132	0.342041	0.313721	0.961114	0.666161	0.571575
bifurcation between pulsed- and stationary- regime								
12.00	68.317	3.4×10^{-4}	1.1×10^{-8}	0.477783	0.477783	0.955033	0.679307	0.679304
12.50	71.164	$< 10^{-8}$	$< 10^{-16}$	0.500644	0.500644	0.500644	0.697104	0.697104
13.00	74.010	$< 10^{-8}$	$< 10^{-16}$	0.499924	0.499924	0.499924	0.713433	0.713433
13.50	76.857	$< 10^{-8}$	$< 10^{-16}$	0.499232	0.499232	0.499232	0.728466	0.728466
14.00	79.704	$< 10^{-8}$	$< 10^{-16}$	0.498535	0.498535	0.498535	0.742350	0.742350

Curves (1) and (2) show a sharper bifurcation from stationary to pulsed regime, since numerical simulations have been performed up to 16384 roundtrips (in the transition region) in order to better approach the asymptotic regime. The mean reflectivity $\langle|A_S(0,t)|^2\rangle/|A_p(0)|^2$ (top curve) even presents an appreciable jump at the bifurcation for both curves (1) and (2), which is smoothed for curves (3) to (6) since simulations have been performed only up to 4096 roundtrips.

Another interesting Brillouin pulse parameter is its width (figures 16 and 17). The reached minimum value is roughly 100 ns, the same for the different R_{eff} and covering a large domain of pump power or of Stokes pulse energy: it means that between 10 and 15 longitudinal modes are then locked. This width increases near the nonlinear threshold, the pump being therefore too weak to excite the side modes, far from the center of the Brillouin gain curve. A width increasing is also observed near the bifurcation towards the stationary regime, but not so clearly and with much more fluctuations in the experimental

12

recording; in this last case, it is the pump nonlinear depletion which doesn't allow the side modes excitation.

Our experiments and the corresponding numerical simulations show also that the roundtrip time decreases uniformly *vs.* pump power or energy per pulse (figures 18 and 19), which corroborates our theoretical prediction that in the vicinity of the nonlinear threshold, the pulse are subluminous, but superluminous near the bifurcation [6]. The lack of a flat zone in these curves clearly shows that the nonlinear interaction can never be neglected. Note also that for a given energy per pulse, the roundtrip time is decreasing when R_{eff} (experimental) or R (numerical) increases.

6. Conclusion

It appears therefore that the experimental results fit the numerical predictions very accurately. The good quantitative agreement for all the experimentally accessible values show that the homogeneous broadening model (1) remains the pertinent Brillouin model for a cw-pumped fiber ring cavity, in spite of some recent criticisms [12] [13]. However, despite of numerous precautions, experiments exhibit large remaining fluctuations. This cannot obviously be surprising near the bifurcation, where numerical simulations show the huge asymptotic regime sensitiveness to the slightest variations of the experimental parameters, as well as the extreme length of the transient regimes, but we expected elsewhere a much more stable behavior. A first explanation is of course related to the intrinsic pump laser instability, which results in non negligible fluctuations of the nonlinear regime, added to the fact that every part of the set-up is not polarization-maintaining.

However there is probably a more fundamental reason due to the interaction with the guided acoustic wave Brillouin scattering (GAWBS) effect. We have indeed observed that the most stable pulsed regimes remained unchanged for some 10 or 100 ms only. Randomly are appearing trains of some 10 pulses much stronger and narrower (by a

typical factor of $\simeq 10$); we attribute these new features to the interaction with the fiber transverse acoustic resonances through cladding Brillouin scattering (CBS). The coupling of the Brillouin transverse resonator with the Brillouin axial resonator is responsible for unstable dynamics, since all kind of transverse resonances may be excited. The pulses are either compressed, for certain cooperative frequencies, or widen and/or destabilized for other frequencies [14].

In Part II. paper, we will overcome the experimentally unstable behavior by the action of an axial intracavity phase modulator whose frequency and strength may be controllably tuned. The resulting controlled coupling reveals now a rich dynamics which is comparable to the SBS-CBS dynamics, but which is still described by the coherent three-wave model. Besides the compressed and/or unstable frequency domains we will obtain - within finite frequency bands - a splitting of the Brillouin solitons in N stable pulses by tuning the phase modulator to *a little smaller N* times the roundtrip frequency.

References

[1] J. Botineau, C. Leycuras, C. Montes, and E. Picholle, *Stabilization of a stimulated Brillouin fiber ring laser by strong pump modulation*, J. Opt. Soc. Am. B **6**, 300-312 (1989).

[2] I.L. Fabelinskii, *Stimulated molecular scattering of light*, in *Molecular scattering of light*, (Plenum, New York 1968), pp.483-532.

[3] W. Kaiser and M. Maier, *Stimulated Mandelstam-Brillouin process*, in *Laser Handbook 2*, T.F. Arecchi and F.O. Schulz-Dubois, eds. (North-Holland, Amsterdam, 1972), p.1077.

[4] E. Picholle, C. Montes, C. Leycuras, O. Legrand, and J. Botineau, *Observation of dissipative superluminous solitons in a Brillouin fiber ring laser*, Phys. Rev. Lett. **66**, 1454-1457 (1991).

[5] C. Montes, A. Mamhoud, and E. Picholle, *Bifurcation in a cw-pumped Brillouin fiber-ring laser: coherent soliton morphogenesis*, *Phys. Rev. A* **49**, 1344 (1994).

[6] C. Montes, D. Bahloul, I. Bongrand, J. Botineau, G. Cheval, A. Mamhoud, E. Picholle, and A. Picozzi, *Self-pulsing and dynamic bistability in cw-pumped Brillouin fiber ring lasers*, J. Opt. Soc. Am. B **16**, 932 (1999), and references therein.

[7] G.P. Agrawal, *Nonlinear Fiber Optics*, Academic Press 2001, 3rd ed., pp.355-384.

[8] J. Botineau, *Interactions non linéaires dans les fibres optiques* in *Physique et technologie des fibres optiques* ed. by Jean-Pierre Meunier, Hermes-Science (Paris 2003) pp.319-332.

[9] I. Bar-Joseph, A.A. Friesem, E. Lichtman, and R.G. Waarts, *Steady and relaxation oscillations of stimulated Brillouin scattering in single-mode optical fibers*, J. Opt. Soc. Am. **2**, 1606 (1985).

[10] S. Randoux and J. Zemmouri *Polarization dynamics of a Brillouin fiber ring laser*, Phys. Rev A **59**, 1644-1552 (1999).

[11] V. Grimalsky, S. Koshevaya, G. Burlak, and B. Salazar-H., *Dynamic effcts of the stimulated Brillouin scattering in fibers due to acoustic diffraction*, J. Opt. Soc. Am. B **19**, 689 (2002).

[12] V.I. Kovalev and R.G. Harrison, *Observation of Inhomogeneous Spectral Broadening of Stimulated Brillouin Scattering in an Optical Fiber*, Phys. Rev. Lett. **85**, 1879-1882 (2000).

[13] V.I. Kovalev and R.G. Harrison, *Waveguide-induced inhomogeneous spectral broadening of stimulated Brillouin scattering in optical fiber*, Opt. Lett. **27**, 2022-2024 (2002).

[14] I. Bongrand, C. Montes, E. Picholle, J. Botineau, A. Picozzi, G. Cheval, and D. Bahloul, *Soliton compression in Brillouin fiber lasers*, Opt. Lett. **19**, 1475 (2001).
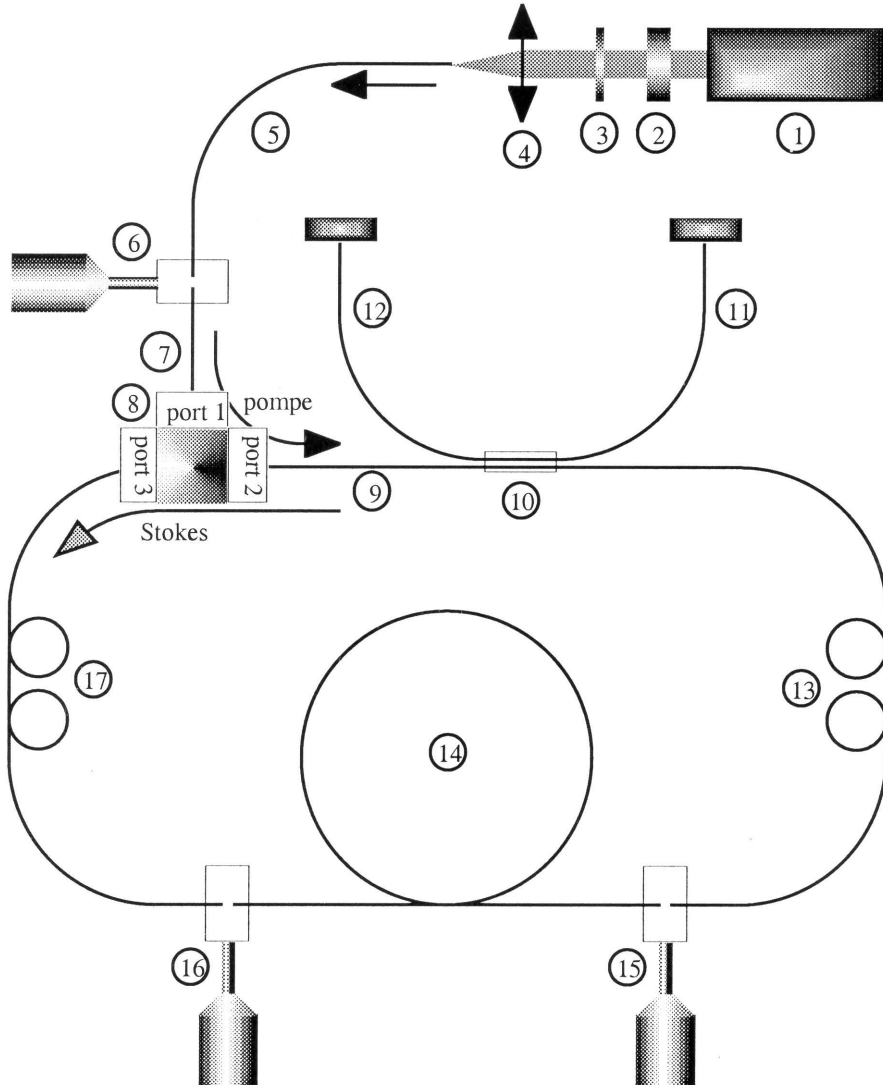
Figure 1: Experimental set-up: (1): diode pumped YAG:Nd^{+++} cw laser (1.319 μm, 340 mW); (2): Faraday isolator: (3): half-wave plate; (4): coupling lens; (5): coupling fiber; (6): microhandler; (7): input fiber; (8): 3-port optical circulator; (9): up-stream fiber; (10): 10/90 coupler ; (11): pump signal detection; (12): Stokes signal detection; (13): polarization controller; (14): single-mode polarization-maintaining fiber; (15, 16): microhandlers; (17): polarization controller.
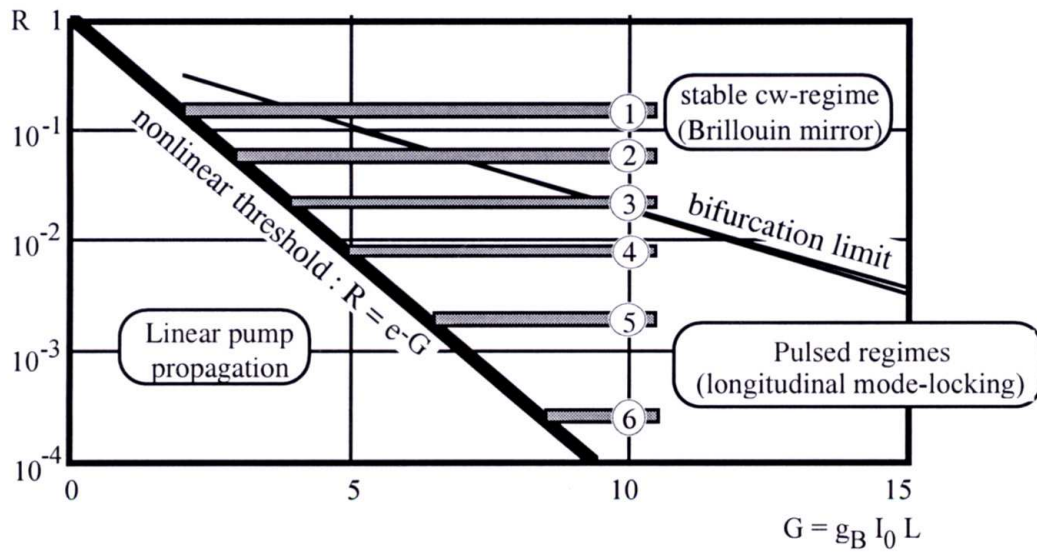
Figure 2: Bifurcation diagram of the Brillouin fiber ring laser with the experimentally explored areas (tinted areas).
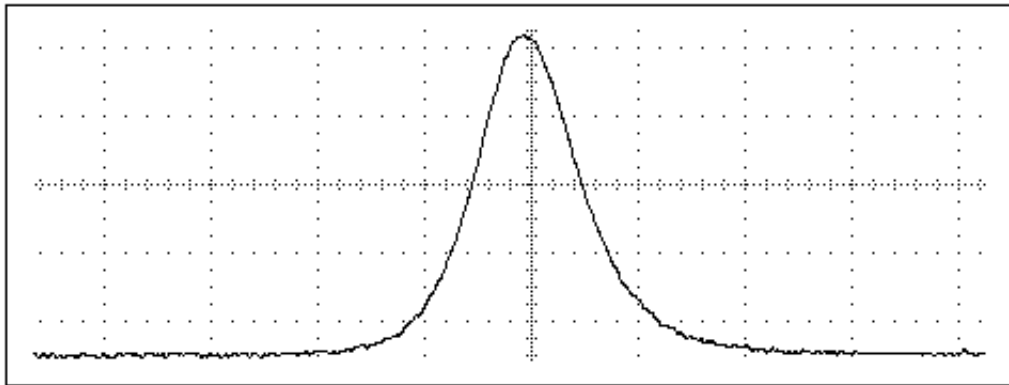
Figure 3: Experimental Brillouin pulse.

roundtrip time

Stokes Signal

roundtrip time

current
width 470.010ns   period 1.19712µs   Vamptd 98.4375mV

current
width 200.753ns   period 630.000ns   Vamptd 153.125mV

Destabilization of the stationary regime by
the adjacent longitudinal mode

Destabilization of the stationary regime by
the second longitudinal mode

(Oscillations on the cw-signal)
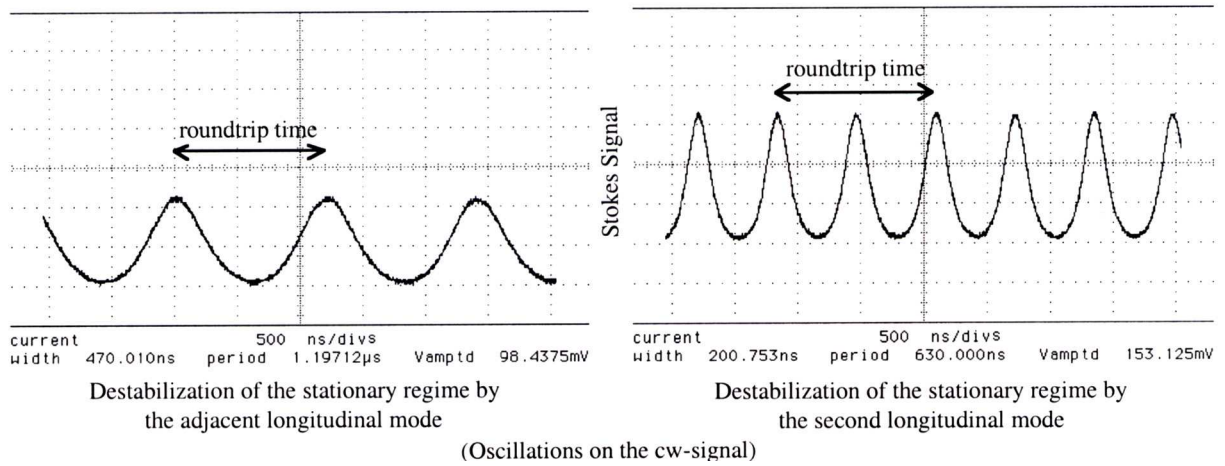
Figure 4: Two experimental examples of destabilization of the cw-regime.

current
width 162.010ns   period 1.25400µs   Vamptd 225.000mW

current
width 167.510ns   period 1.24350µs   Vamptd 250.000mW
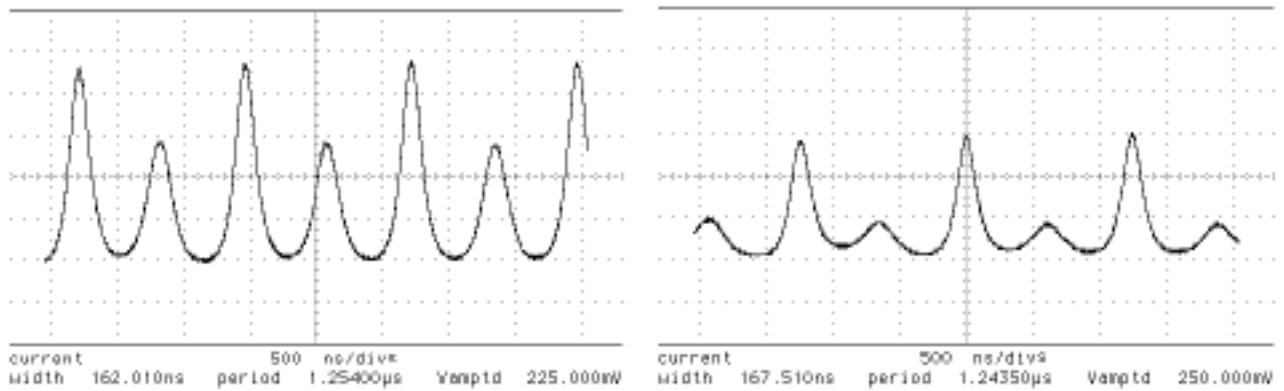
Figure 5: Experimental building of the Stokes pulse from the second mode destabilization.

current
width 242.310ns   period 1.21230μs   Yamptd 340.625mW

current
width 77.365 ns   period 1.25854μs   Yamptd 843.750mW
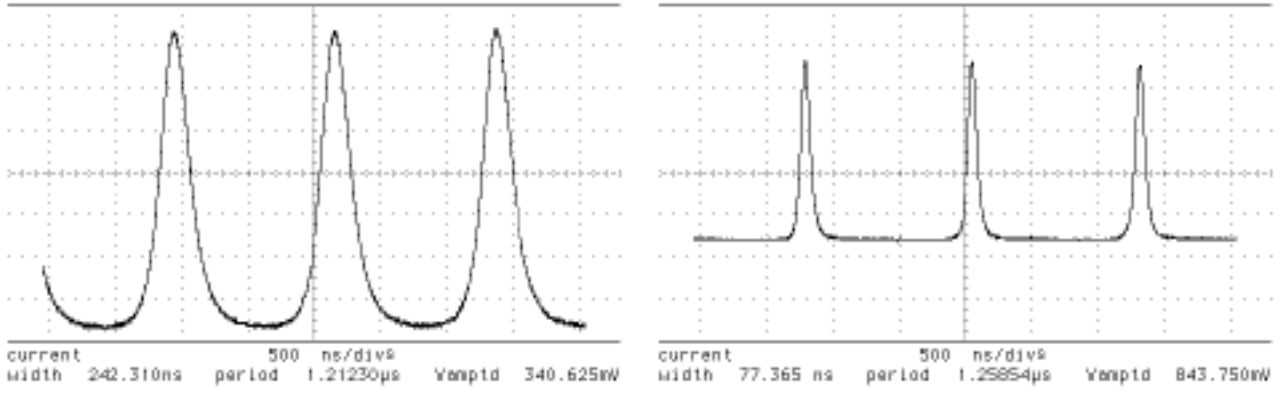
Figure 6: Experimental simultaneous strengthening and narrowing of the Stokes pulse when the pump power is decreasing from the bifurcation point between the cw-regime and the pulsed regime.

current
width 151.930ns   period 1.27019μs   Yamptd 48.4375mW

current
width 206.160ns   period 1.27361μs   Yamptd 13.4375mW
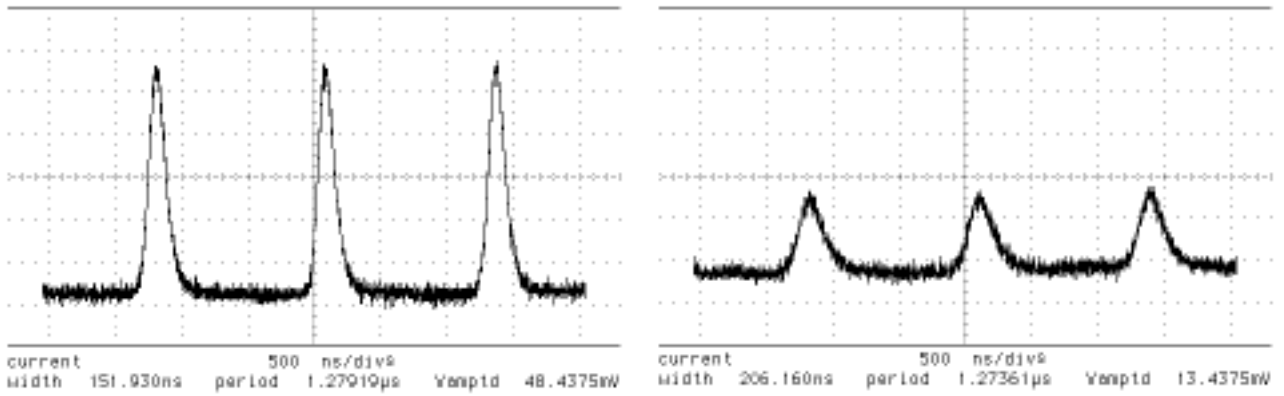
Figure 7: Experimental Stokes pulses evolution when the pump power is decreasing up towards the nonlinear Brillouin threshold.
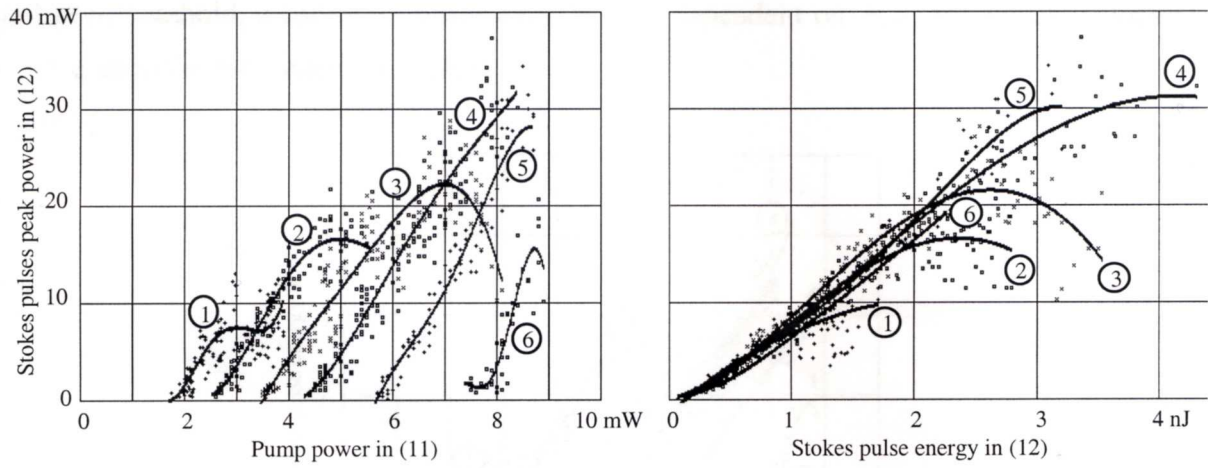
Figure 8: Experimental Stokes pulse peak power for the different R_{eff} values *vs.*pump power (left); and *vs.*energy per pulse (right).
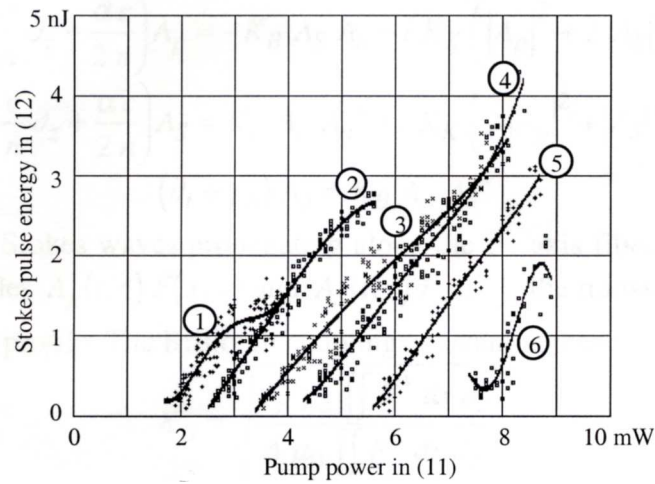
Figure 9: Experimental Stokes pulse energy *vs.* pump power.
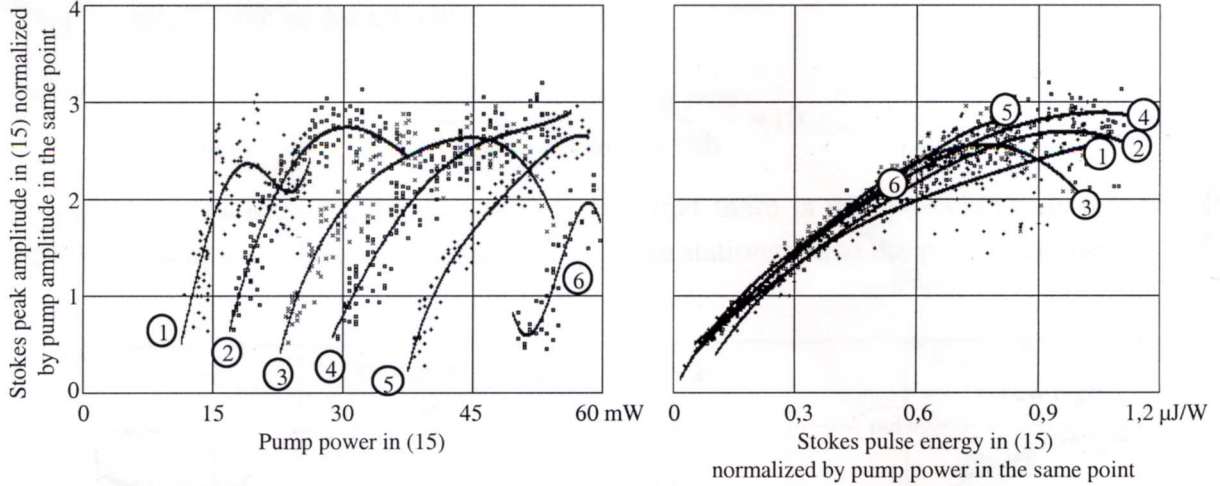
Figure 10: Experimental normalized Stokes peak amplitude in (15) for the different values of R_{eff} *vs.* pump power in this point (left)and *vs.* normalized Sokes energy (right).
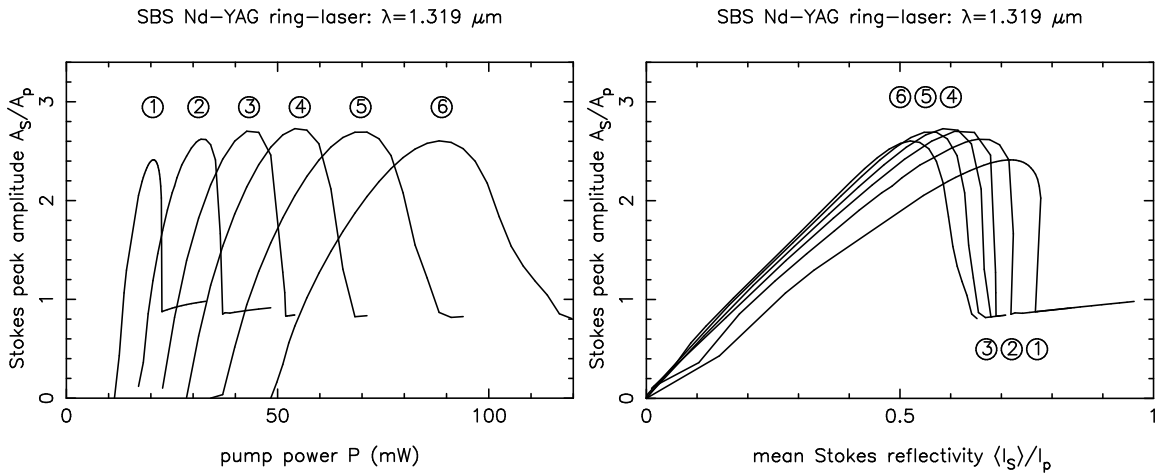
Figure 11: Numerical simulation of Eqs.(1): Normalized Stokes peak amplitude at $z = 0$ *vs.* input pump power in mW (left) and *vs.* normalized mean Stokes reflectivity $\langle |A_S(0,t)|^2 \rangle / |A_p(0)|^2$ (right).
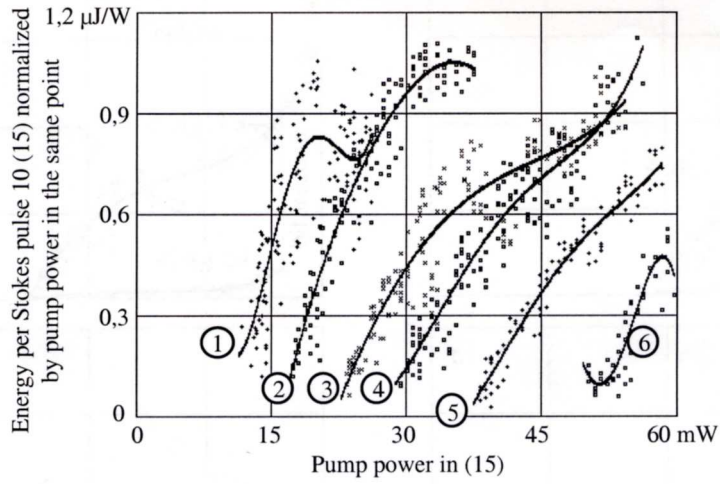
Figure 12: Experimental normalized Stokes pulse energy in (15) *vs.* pump power in this point.
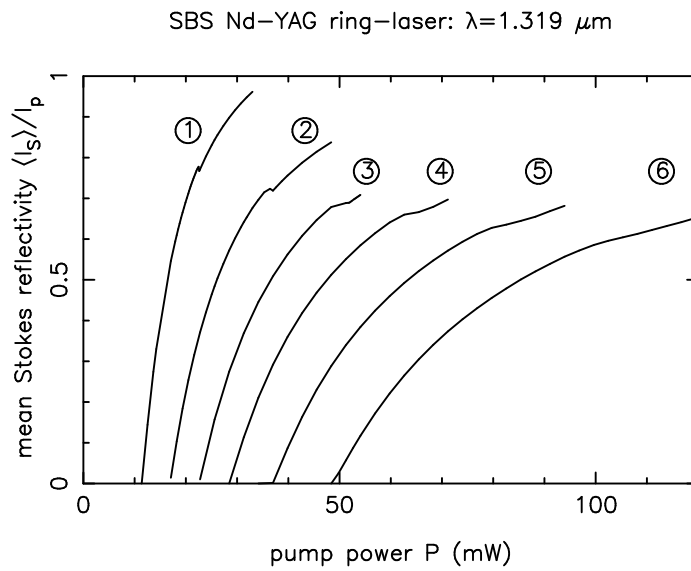
Figure 13: Numerical simulation of Eqs.(1): Normalized mean Stokes reflectivity $\langle|A_S(0,t)|^2\rangle/|A_p(0)|^2$ *vs.* input pump power in mW.
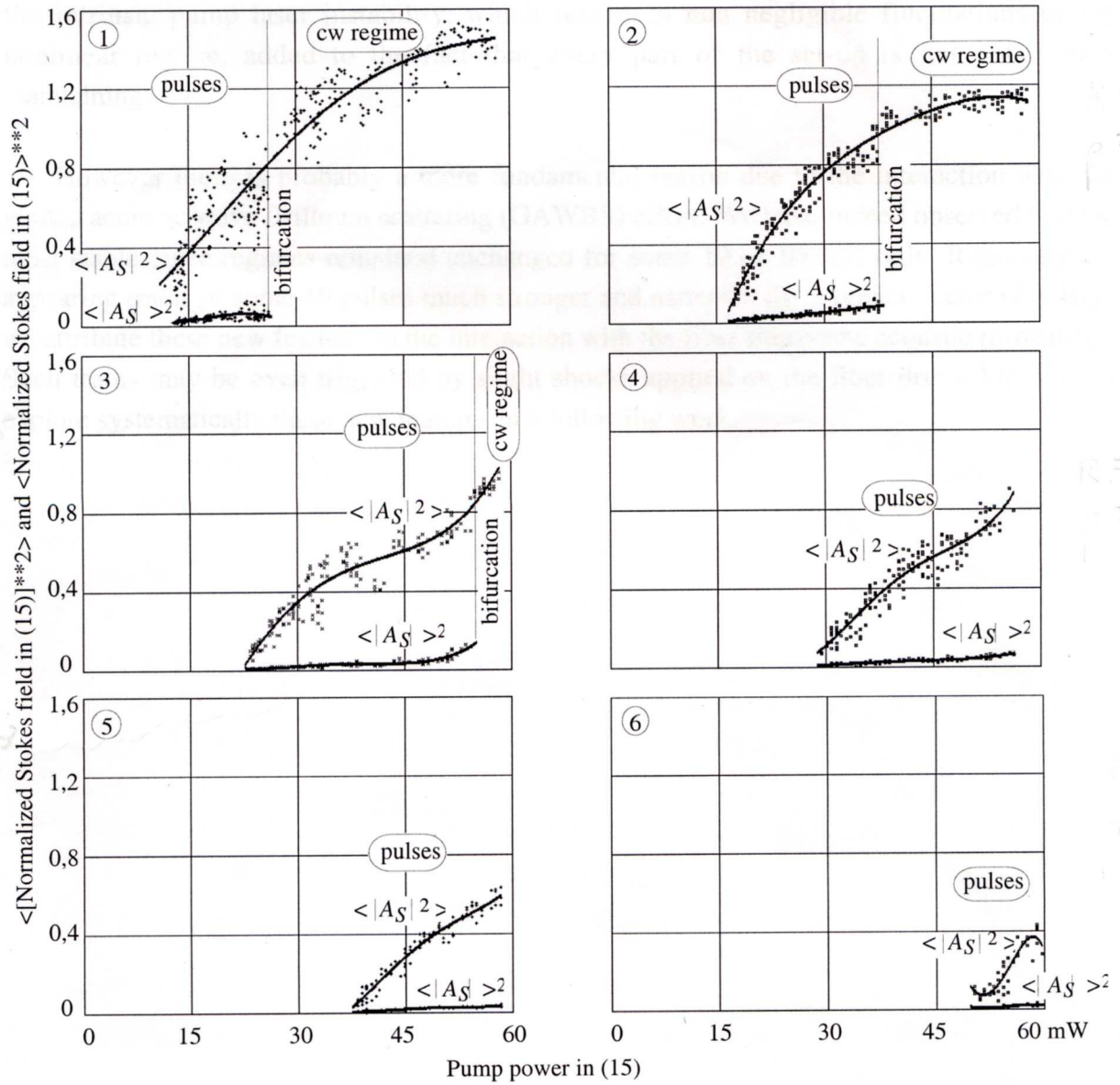
Figure 14: Comparison between the averaged normalized Stokes amplitude square and of the square of the averaged normalized Stokes amplitude in (15) vs pump power in this point for the different values of R_{eff}.
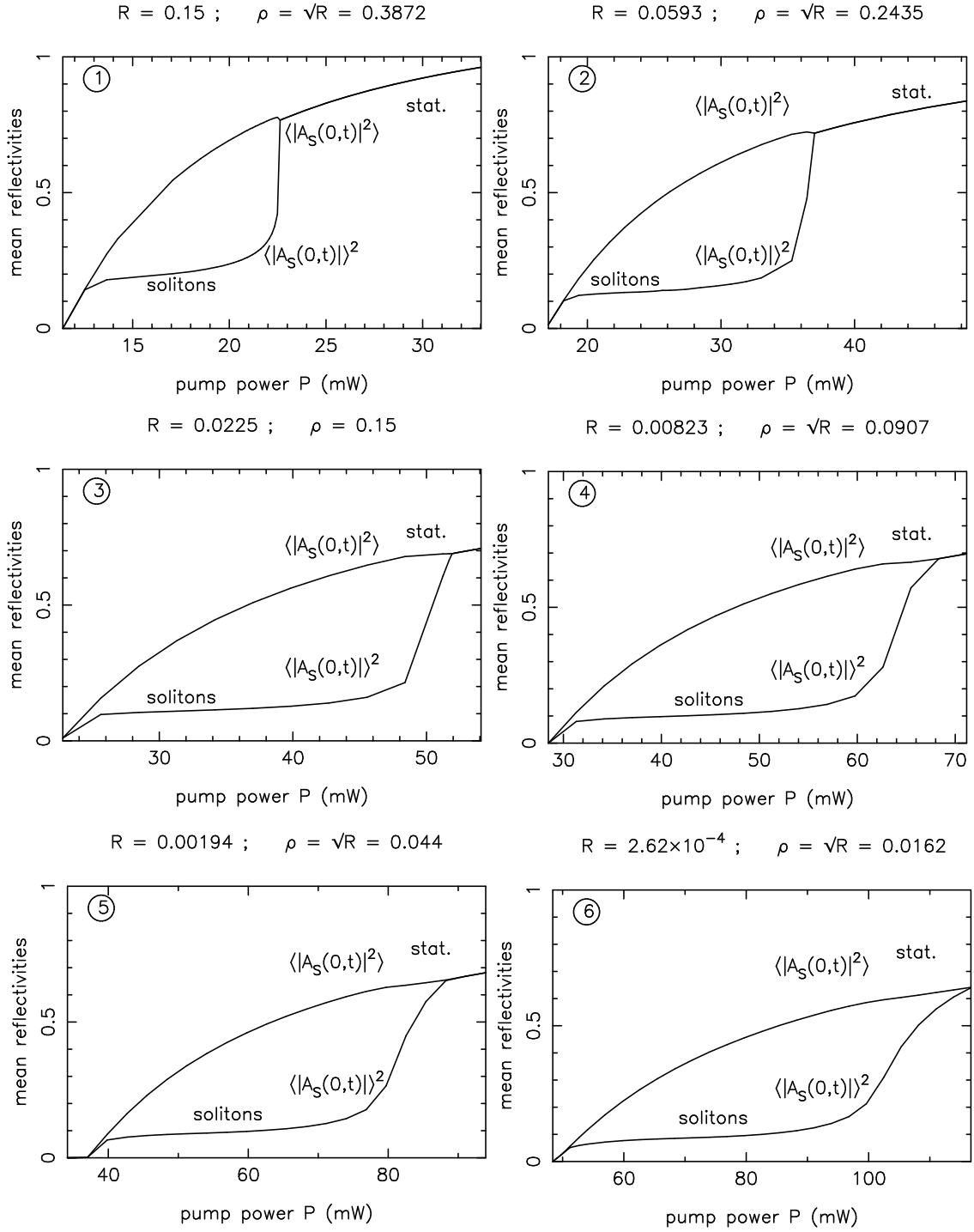
Figure 15: Mean reflectivities $\langle |A_S(0,t)|^2\rangle/|A_p(0)|^2$ and $\langle |A_S(0,t)|\rangle^2/|A_p(0)|^2$ as function of cw-pump power, obtained by numerical simulation of Eqs.(1), for (1) $R = 0.15$; (2) $R = 0.0593$; (3) $R = 0.0225$; (4) $R = 0.00823$; (5) $R = 0.00194$; and (6) $R = 2.62 \times 10^{-4}$. The soliton localisation domain of the bifurcation map is characterized by a low value of the square averaged Stokes amplitude $\langle |A_S(0,t)|\rangle^2$ with respect to the averaged square Stokes amplitude $\langle |A_S(0,t)|^2\rangle$.
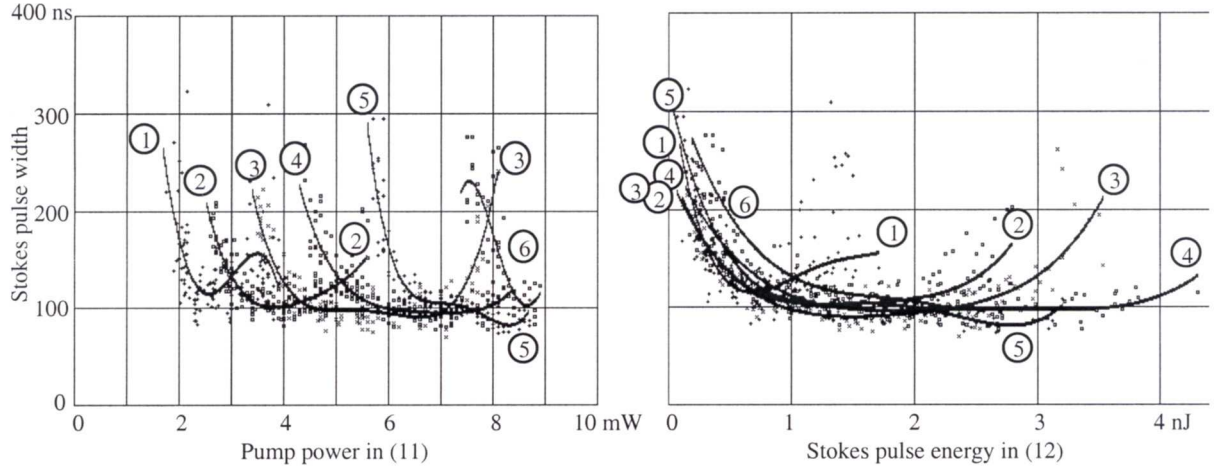
Figure 16: Experimental Stokes pulse FWHM for the different R_{eff} *vs.* pump power (left); and *vs.* energy per pulse (right).
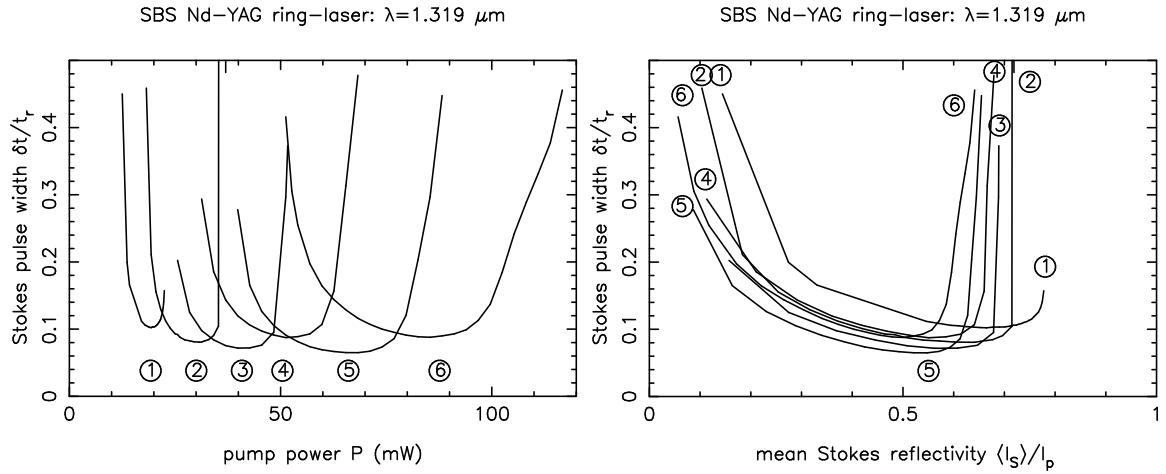

Figure 17: Numerical simulation of Eqs.(1): Stokes intensity pulse width at $z = 0$ normalized to the linear flight time $\delta_t |A_S(0,t)|^2/t_r$ *vs.* input pump power in mW (left) and *vs.* normalized mean Stokes reflectivity $\langle |A_S(0,t)|^2 \rangle / |A_p(0)|^2$ (right).
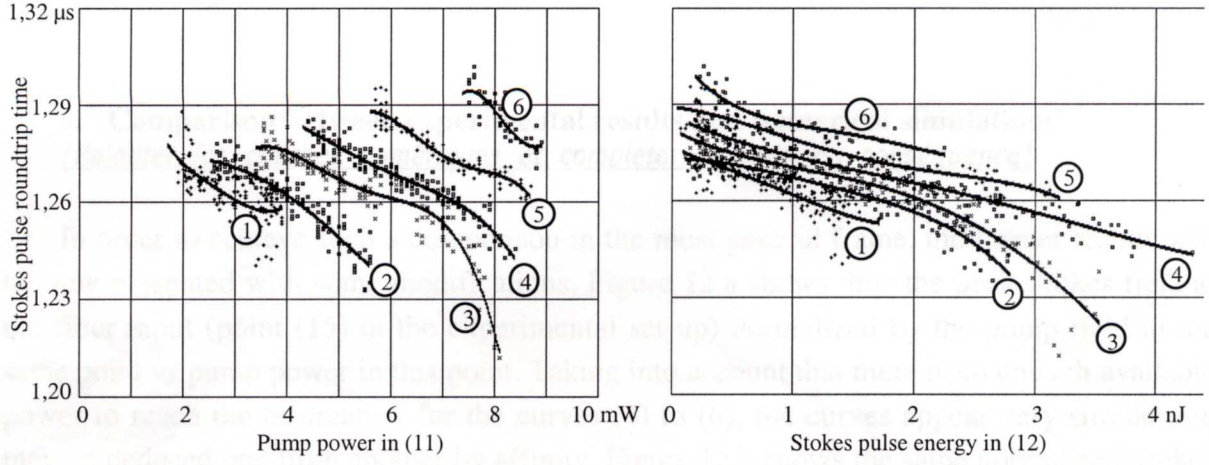
Figure 18: Experimental Stokes pulse roundtrip time for the different values of *vs.* pump power (left); and *vs.* energy per pulse (right).
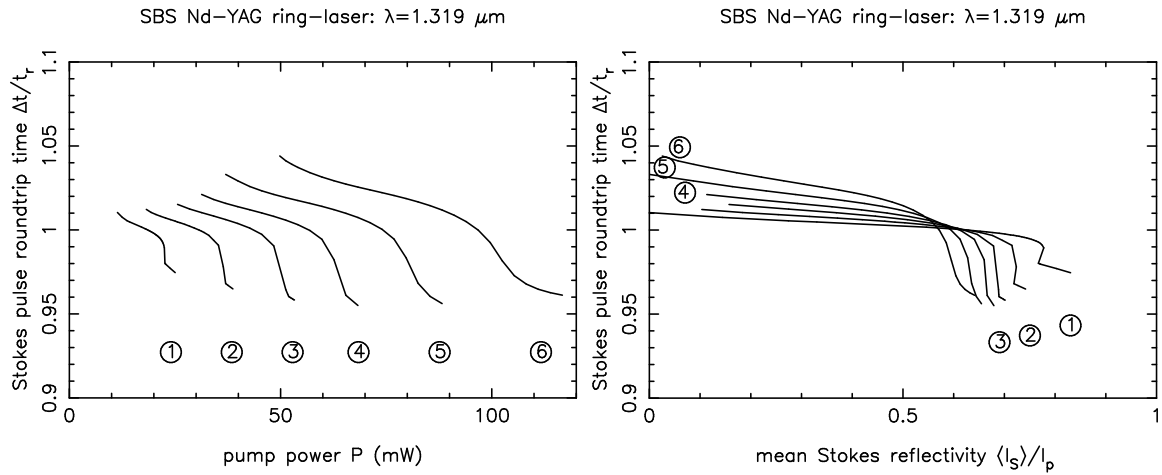

Figure 19: Numerical simulation of Eqs.(1): Stokes pulse roundtrip time at $z = 0$ normalized to the linear flight time $\delta_t|A_S(0,t)|^2/t_r$ *vs.* input pump power in mW (left) and *vs.* normalized mean Stokes reflectivity $\langle|A_S(0,t)|^2\rangle/|A_p(0)|^2$ (right).